

Tunable coupling of a quantum phononic resonator to a transmon qubit with flip-chip architecture

Xinhui Ruan,^{1,2,3,a)} Li Li,^{1,4,a)} Guihan Liang,^{1,4} Silu Zhao,^{1,4} Jia-heng Wang,⁵ Yizhou Bu,^{1,4} Bingjie Chen,^{1,4} Xiaohui Song,¹ Xiang Li,^{1,4} He Zhang,^{1,4} Jinzhe Wang,^{1,4} Qianchuan Zhao,² Kai Xu,^{1,6} Heng Fan,^{1,4,6} Yu-xi Liu,⁵ Jing Zhang,^{7,8} Zhihui Peng,^{3,6} Zhongcheng Xiang,^{1,4,6,9} and Dongning Zheng^{1,4,6,9}

¹⁾Beijing National Laboratory for Condensed Matter Physics, Institute of Physics, Chinese Academy of Sciences, Beijing 100190, China

²⁾Department of Automation, Tsinghua University, Beijing 100084, P. R. China

³⁾Key Laboratory of Low-Dimensional Quantum Structures and Quantum Control of Ministry of Education, Key Laboratory for Matter Microstructure and Function of Hunan Province, Department of Physics and Synergetic Innovation Center for Quantum Effects and Applications, Hunan Normal University, Changsha 410081, People's Republic of China

⁴⁾School of Physical Sciences, University of Chinese Academy of Sciences, Beijing 100049, China

⁵⁾School of Integrated Circuits, Tsinghua University, Beijing 100084, China

⁶⁾Hefei National Laboratory, Hefei 230088, China

⁷⁾School of Automation Science and Engineering, Xi'an Jiaotong University, Xi'an 710049, China

⁸⁾MOE Key Lab for Intelligent Networks and Network Security, Xi'an Jiaotong University, Xi'an 710049, China

⁹⁾CAS Center for Excellence in Topological Quantum Computation and School of Physical Sciences, University of Chinese Academy of Sciences, Beijing 100049, China

(*Electronic mail: dzheng@iphy.ac.cn)

(*Electronic mail: zcxiang@iphy.ac.cn)

(*Electronic mail: zhihui.peng@hunnu.edu.cn)

(Dated: 30 April 2024)

A hybrid system with tunable coupling between phonons and qubits shows great potential for advancing quantum information processing. In this work, we demonstrate strong and tunable coupling between a surface acoustic wave (SAW) resonator and a transmon qubit based on galvanic-contact flip-chip technique. The coupling strength varies from $2\pi \times 7.0$ MHz to $-2\pi \times 20.6$ MHz, which is extracted from different vacuum Rabi oscillation frequencies. The phonon-induced ac Stark shift of the qubit at different coupling strengths is also shown. Our approach offers a good experimental platform for exploring quantum acoustics and hybrid systems.

Circuit quantum acoustodynamics (cQAD) studies the interaction between mechanical vibrations and superconducting qubits, which provides a way to control the non-classical mechanical modes (phonons). There are various mechanical degrees of freedom including bulk wave¹, surface acoustic wave (SAW)²⁻⁷ and vibrations of suspended beams⁸⁻¹¹. Among them, SAW is a traveling acoustic wave that propagates on the surface of the solid materials. Confining SAW between the Bragg mirrors can form the Fabry-Perot SAW cavity with achieved quality factor (Q) up to 100000^{12,13}. Compared to circuit quantum electrodynamics (cQED) systems^{14,15}, acoustic waves travel five orders of magnitude slower than electromagnetic waves and the wavelength of gigahertz acoustic waves is close to that of optical waves. Therefore, the cQAD system has various applications, such as phonon-mediated quantum state transfer¹⁶, quantum random access memory¹⁷ and medium for microwave-optical conversion¹⁸⁻²⁰. Some impressive work has been done to study the physical properties of cQAD systems, including preparation of phonon Fock states^{6,21}, splitting of phonons^{22,23}, phonon

induced non-exponential decay of giant atoms²⁴, electromagnetically induced acoustic transparency²⁵, squeezing and entanglement^{10,26} of phonon states.

For cQAD system, compared to weak coupling, strong coupling promises performing more coherent operations between superconducting qubits and other phononic resonators. Strong coupling regime can be achieved by improving the coherence time of the cQAD system or increasing the coupling strength. Fabricating the qubits directly on piezoelectric materials will induce phonon loss channel to the qubits. Therefore, it is better to fabricate the qubit and SAW on two different materials to keep good performance of cQAD system. There are two ways to realize the target. One way involves using piezoelectric films on sapphire substrate and placing the qubit on the area where the piezoelectric films are etched^{27,28}. However, etching could cause damages to the substrate surface. The other option is to utilize flip-chip architecture to assemble two substrates made of different materials^{1,6}. The reported flip-chip technology^{6,7} used in the cQAD system relies on glue. Therefore, the coupling strength between the qubit and SAW cavity is determined by the interchip geometric capacitance or mutual inductance and the grounding plane could be affected by glue bumps.

^{a)}These authors contributed equally to this work.

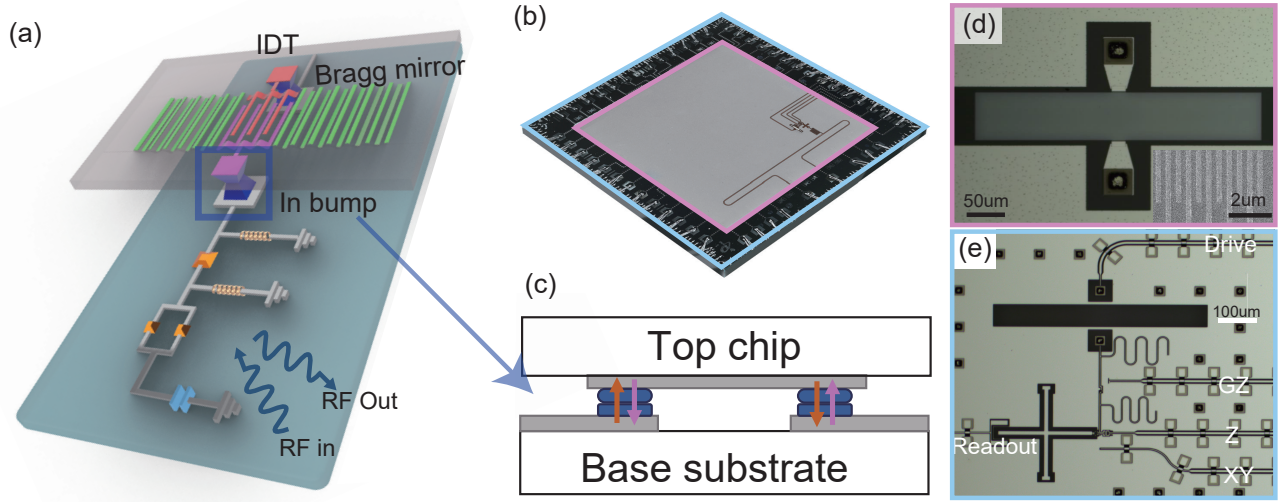


FIG. 1. The Device. (a) The 3D schematic of the sample. The SAW cavity consists of two Bragg mirrors and an IDT. One port of the IDT connects to the transmon qubit with an indium bump and a gmon, while the other port connects to a driven line. The phonon modes of SAW are distributed on the surface of LiNbO_3 . (b) Photograph of the device after flip-chip assembly. The base and top chip size is $15\text{ mm} \times 15\text{ mm}$ and $11\text{ mm} \times 11\text{ mm}$, respectively. (c) Side view of the assembled device. The indium (In) bumps of the top and base chip are compressed together under pressure and allow to realize the galvanic contact. (d) Optical micrograph of the top chip. (e) Optical micrograph of the base chip. The insert shows the scanning electron micrograph of zoomed stripe structures in the SAW cavity.

Here, we report fabrication process and characterizations of the device which couples a GHz-frequency SAW resonator (cavity) to a transmon qubit. The qubit chip and SAW cavity chip are bonded together by flip-chip assembly with galvanic bumps (Indium). We verify the strong coupling between the SAW cavity and the qubit by performing vacuum Rabi oscillations experiment. Due to the existence of a tunable coupler, we can adjust the coupling strength in a range from $2\pi \times 7.0$ to $-2\pi \times 20.6\text{ MHz}$. Then we measure the ac Stark shift of the qubit to show the effect of phonons inside the SAW cavity on the qubit. Our galvanic-connected flip-chip device can be realized with stronger coupling strength while ensuring the coherence of each elements.

Our device, as shown in Fig. 1a, is composed of two chips, which are bonded together using flip-chip technology. The top chip consists of a SAW resonator, fabricated on 128°Y-X lithium niobate (LiNbO_3) substrate – a kind of material with strong piezoelectric effect. The SAW cavity is formed by an IDT (purple and orange) and two Bragg mirrors (green) on both sides. The IDT can conduct the conversion between acoustic waves and microwave, as well as excitation and detection of SAWs. The Bragg mirrors use gratings to form a Fabry-Perot cavity²⁹, which supports a stopband in the frequency response³⁰. The base substrate is sapphire and is used to fabricate qubits and control lines. The reason why we need two kinds of substrate is that the dielectric loss on LiNbO_3 is very large and will cause decoherence of qubits³¹. The artificial atom we use is a frequency-tunable transmon qubit, formed by a DC SQUID and a shunted capacitor. The transmon qubit connects to the SAW cavity through a RF SQUID (i.e. gmon^{32,33}) with tunable inductance and indium bumps, which provides galvanic contact between the top and base

chips. Compared to the designs in Ref.⁶, we do not need to use interchip mutual inductance to make connection, which is sensitive to the space between the chips and has limited values. As show in Fig. 1e, the transmon qubit is controlled by XY lines with the rotation in X or Y axis in the Bloch sphere and Z lines which tunes the transition frequency of qubit by applied flux bias. The state of the transmon qubit is read out by the dispersive-coupling coplanar waveguide resonator.

The fabrication of the device uses electron beam lithography (EBL) and optic laser lithography. First, we use ebeam evaporation to deposit 100nm Al for the base chip and 30nm Al for the top chip, respectively. Then, we use optic lithography and wet etch to form coplanar waveguides (CPWs) and ground planes. The stripes of the SAW cavity in the top chip are defined through EBL with width as $d = 240\text{ nm}$ and length as $75\text{ }\mu\text{m}$ using photoresist PMMA. These slender stripes are extremely difficult to be fabricated, especially when the periodic cell number of the Bragg mirrors at each side is $N_m = 400$ and the periodic cell number of IDT is $N_t = 20$. Before the evaporation process, we conduct the oxygen plasma cleaning in situ to remove the resist residue using *Plassys*. The Al stripes are made by two steps. The first step is to create extra undercuts with the deposition angle at $\pm 80^\circ$ and 30nm Al, facilitating the lift-off process. The second step is to deposit 30nm Al at 0° angle. This deposition method is also used in Ref.⁴. The stripe structures after lift-off are shown in Fig. 1d. The qubits in the base chip are exposed with EBL and fabricated with standard Dolan bridge shadow evaporation. The final step is to make flip-chip architecture using *FC150* bonder. Although indium is a commonly used metal for flip-chip bonding³⁴ and becomes superconductive below 3.4K, the direct contact between aluminum and indium will

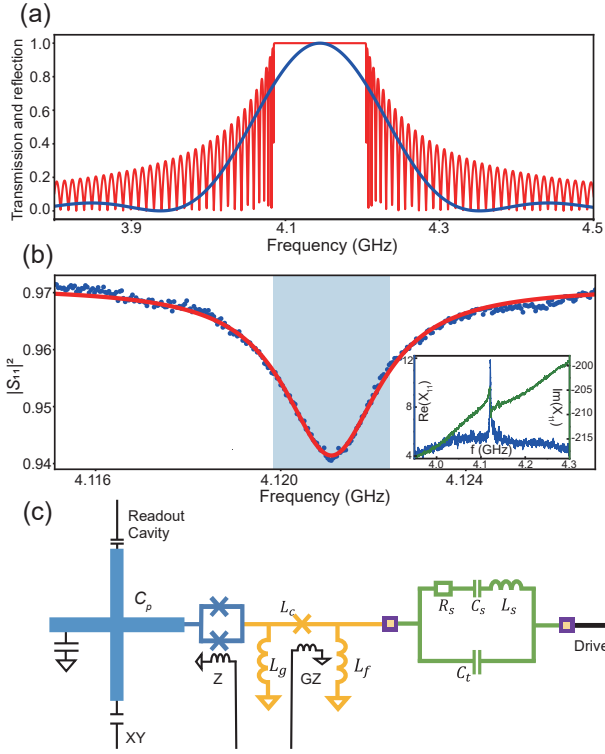


FIG. 2. Modelling of the SAW-Qubit coupling system. (a) The red line is calculated reflection of Bragg mirror and the blue line is the conductance of the IDT. (b) The measured reflection of SAW cavity (blue dots) with Lorentzian fitting (red line). The insert shows the real and imaginary reactance X_{11} of the SAW cavity, calculated from the measured S data. The blue area shows the decay rates of the cavity as $\kappa_{S,RT} = 2.5$ MHz. (c) Circuit diagram of our SAW-Qubit coupling system. The green parts represent the equivalent circuit of SAW cavity, which is distributed in the top LiNbO₃ chip. The gmon coupler (Yellow) and the transmon qubit (blue) are in the base Sapphire chip.

form an intermetallic^{35,36}, damaging the conductivity of these bumps. To address this issue, we use niobium as the diffusion barrier, which can be deposited via magnetron sputtering and also exhibits superconductivity below 9.2 K. Then, we deposit indium on each chips with the thickness of $7.5 \mu\text{m}$ using thermal evaporation. Note that we conduct ion mill in situ to make good electrical contact prior to each metal deposition. The two chips are bonded together with a force of 7000 g, ensuring the distance between them around $7.5 \mu\text{m}$. The complete device is shown in Fig. 1b with the side-view diagram in Fig. 1c.

The frequency response of SAW cavity can be simulated with the coupling-of-mode (COM) model³⁰. The propagation speed of SAW in 128°Y-X LiNbO₃ is $v_a \approx 3979$ m/s at room temperature³⁷. The periodicity of IDT stripes is $p = 4d$ and determines the central wavelength and frequency of the excited acoustic wave as $\lambda_0 = p$ and $f_0 = v_a/\lambda_0$. Both overexposure in EBL and the placed direction of IDT will affect its central frequency because LiNbO₃ is an anisotropic material. The calculated conductance of IDT is a *sinc* function at f_0 with the

bandwidth $\Delta_{IDT} = 184$ MHz, as shown in Fig. 2a. The reflection of single electrode in the Bragg mirror is $|r_{s1}| = 0.045$. We need to conduct the Bragg mirror with a stripe array, in order to improve the total reflection rate to 1 by using the interference among them. The bandwidth of Bragg mirror is $\Delta_M = 120$ MHz, which should be less than Δ_{IDT} , and is used to select frequency and improve Q factor.

We show the measured reflection data of the SAW cavity with $N_t = 20$ and the distance between the two Bragg mirrors $L_0 = 20.5\lambda$ in Fig. 2b. The equivalent inductance can be calculated with $L_s = 0.5 \lim_{\omega \rightarrow \omega_0} \text{Im}[\partial X/\partial \omega]$, where the reactance X in the insert can be calculated from the measured S data and $\omega_0 = 2\pi f_0$. The calculated BVD parameters of the SAW cavity in Fig. 2b are $L_s = 186$ nH, $C_s = \omega_0^2/L_s = 8$ fF and $R_s = Z_s/Q_s = 2.92 \Omega$ with the characteristic impedance $Z_s = \sqrt{L_s/C_s}$ and the room temperature Q factor $Q_{S,R} = 1643$. The electrostatic capacitance of IDT is $C_t = 744$ fF.

To study the cQAD system in the quantum regime, we mount the sample inside the mixing chamber of a dilution refrigerator with base temperature around 10 mK. The transmon qubit can be described by the charge energy $E_c/h = e^2/C_p = 0.18$ GHz with $C_p = 108$ fF and maximal Josephson energy $E_{j0}/h = 22.5$ GHz. The transition frequency from ground to first-excited state of the qubit can be turned by external flux Φ_e as $\omega_q = (\sqrt{E_c E_{j0} \cos(\Phi_e/\Phi_0)} - E_c)/\hbar$ with $\Phi_0 = h/2e$. The Hamiltonian of the system shown in Fig. 2c can be described by Jaynes-Cummings model as

$$H = \omega'_0 a^\dagger a + \frac{\omega_q}{2} \sigma_z + g_c (a^\dagger \sigma_- + a \sigma_+), \quad (1)$$

where a is the annihilation operator of SAW cavity mode, σ_- (σ_+) is the annihilation (creation) operator and σ_z is the population operator of the transmon qubit. ω'_0 is the resonance frequency of SAW cavity at low temperature. g_c is the coupling strength between SAW cavity and qubit and is adjustable as

$$g_c = \frac{1}{2} \frac{1}{\sqrt{(L_J + L_g)(L_s + L_f)}} \frac{L_g L_f}{L_g + L_f + L_c} \omega'_0, \quad (2)$$

where $L_c = L_{c0}/\cos \delta$ is the tunable inductance of gmon and δ is the phase difference across the junction, tuned by the DC bias in the RF SQUID. The parameters of the gmon loop are $L_g = 475$ pH, $L_f = 523$ pH and $L_{c0} = 645$ pH, which are obtained by the measured coupling strengths (discussed later). L_J is the inductance of the transmon qubit, which is around 10 nH and can be tuned by the external flux.

Figure 3a shows how the transition frequency of qubit is modulated by the bias of gmon. The applied voltage converts to biased current in the local control lines on chip because of the series resistors in the input lines. The effective inductance of gmon changes with the bias voltage and affects the transition frequency of qubit. Moreover, the applied voltage to gmon causes Z-crosstalk to the qubit. After correcting, the modulated curve is shown in Fig. 3b.

We prepare the qubit to excited state $|e\rangle$ (denote ground and excited state of qubit as $|g\rangle$ and $|e\rangle$), the Fock state of SAW cavity as $|0\rangle, |1\rangle$) then track the time-domain response of the qubit

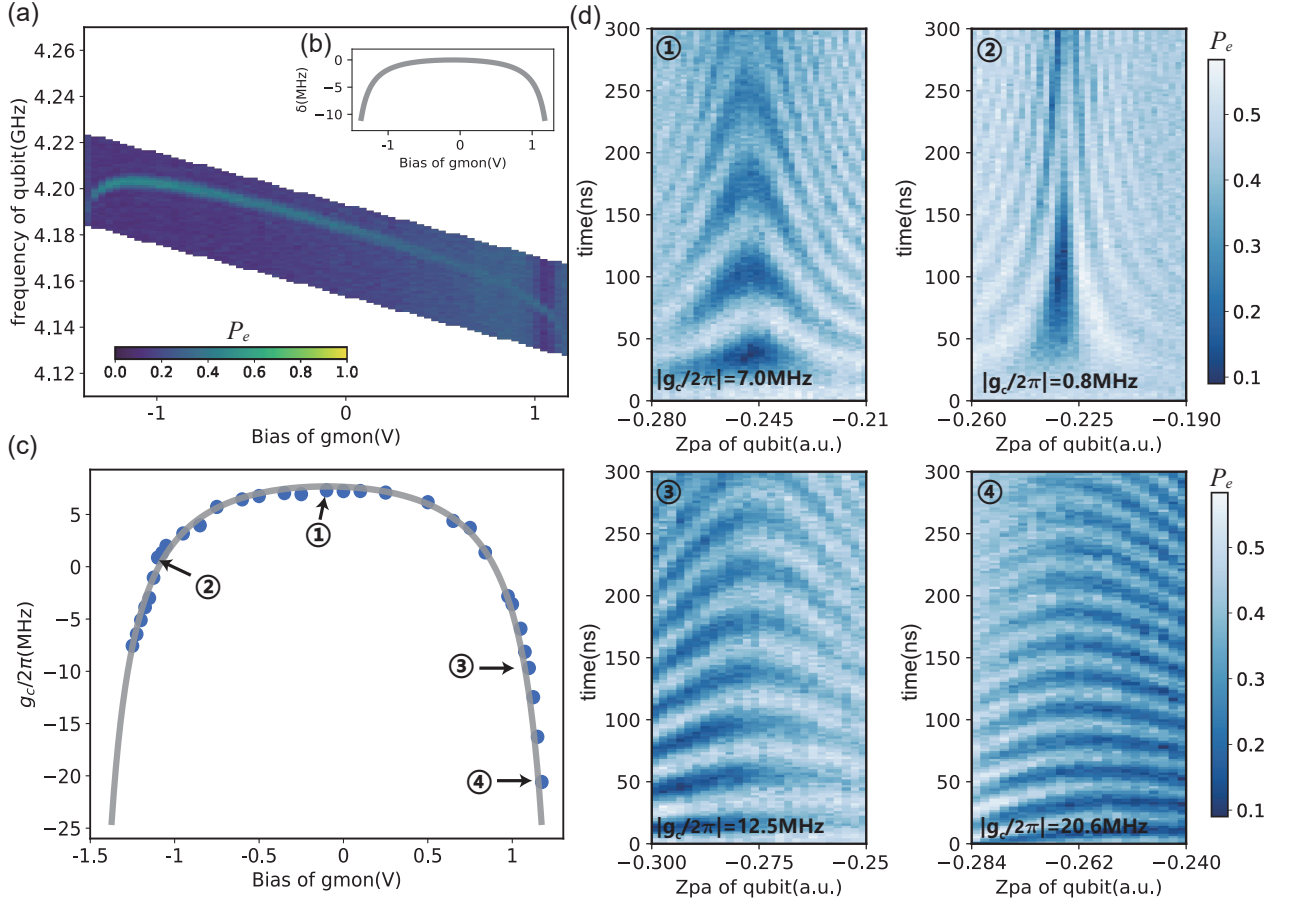


FIG. 3. Characterization of tunable coupling between the SAW cavity and qubit via gmon. (a) The two-dimensional energy spectrum of qubit under different gmon biases. The fitting data after removing the influence of crosstalk is shown in (b). (c) The coupling strength of the SAW cavity and qubit under different gmon biases, and the curve morphology is consistent with (b). The blue dots are experimental data. (d) The time-domain oscillation data from points ①-④ in (c).

over a narrow range around the frequency of SAW cavity by qubit fast Z-control pulse. As the qubit bias is moved to resonance with SAW cavity causing oscillation between dressed states $|0e\rangle$ and $|1g\rangle$, we expect the beating frequency to decrease to $2g_c$ as shown in Fig. 3d. The frequency of SAW cavity can be obtained as $\omega'_0/2\pi = 3.901$ GHz. We conduct experiments under different gmon biases in Fig. 3c to investigate the variation of qubit-SAW cavity coupling strength with gmon bias. Fig. 3d①-④ presents the Rabi oscillations of different effective coupling strength obtained in our measurements, Fig. 3d④ shows a maximum $g_c/2\pi = 20.6$ MHz.

The pulse sequence for the measurement of the phonon's energy relaxation time (T_{1S}) in SAW cavity is depicted in Fig. 4a. The qubit is excited with X gate while off-resonance, and then coupled to the SAW cavity for 40 ns to transfer the state with an iSWAP. A second iSWAP later retrieves the state back to qubit for readout. The resulting decay in Fig. 4b gives the lifetime of a single phonon in SAW cavity yields $T_{1S}^{Meas} \approx 205$ ns.

The entire relaxation process can be divided into three parts: the first iSWAP gate, the delay and the second iSWAP gate, as denoted in Fig. 4a. The dissipation experienced by

the system during the swap process is contributed by both the qubit and the cavity, depending on their individual dissipation rates γ_q^{swap} and γ_s , respectively. On the other hand, the qubit and SAW cavity are in a large detuning during the delay, introducing a Purcell effect $\gamma_s^* = \gamma_s + (g_c/\Delta)^2 \gamma_q^{idle}$ for SAW cavity, where $\Delta = \omega_q - \omega'_0$ and γ_q^{idle} is the dissipation rates of qubit at idle frequency. Two iSWAP gates only change the initial value of the curve so the population of SAW cavity being in the entire process is denoted as

$$P_1^{SAW}(t) = P_0 \cdot e^{-t \cdot [\gamma_s + (g_c/\Delta)^2 \gamma_q^{idle}]} \quad (3)$$

According to the experimental parameters in Fig. 4b and Fig. 4d, the additional dissipation caused by the Purcell effect is much smaller than intrinsic dissipation, i.e. $(g_c/\Delta)^2 \gamma_q^{idle} \ll \gamma_s$. Therefore, the T_{1S} we measured is reliable which allows the determination of the quality factor $Q^{SAW} = \omega'_0 \cdot T_{1S} \approx 5025$. The T_2 of SAW cavity can be measured by the pulse sequence shown in Fig. 4d which is similar to the case of T_1 . Figs. 4e and 4f show the measured data of SAW cavity and the qubit at the idle point, respectively.

Finally, we used the ac Stark effect to calibrate the phonon

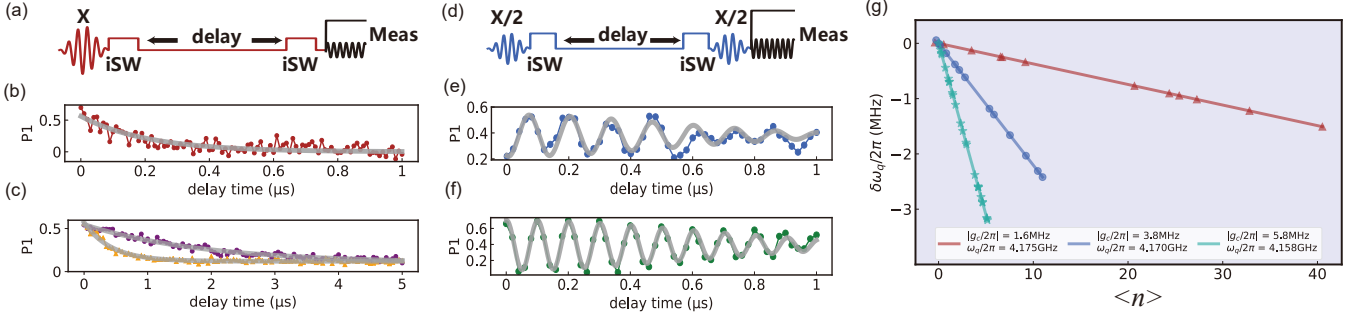


FIG. 4. The characterization of the phonon in SAW cavity. (a) The pulse sequence for the measurement of the phonons' energy relaxation time T_{1S} . X means the X gate for qubit. (b) The red dots represent the data obtained from experimental measurements, while the gray curve represents the fitted data. (c) Decoherence time of qubit at different frequencies. The T_1 of the qubit at the swap point is illustrated with orange points, measured as $T_{1q}^{swap} \approx 1881$ ns when the coupling is turned off. The T_1 of the qubit at the idle point is shown with purple points, measured as $T_{1q}^{idle} \approx 452$ ns. (d) The pulse sequence for the measurement of the phonons' dephasing time T_{2S} . X/2 means the X/2 gate for qubit. (e) The measured data of T_{2S} is illustrated with blue points and the gray curve is fitting data. (f) The measured data of T_{2q} at idle frequency is illustrated with green points and the gray curve is fitting data. (g) Characterize the number of phonons in the SAW cavity using the ac Stark effect at different coupling strengths.

number in the SAW cavity. According to the results of c-QED in dispersive regime, the frequency of the qubit varies with the number of phonons in the cavity

$$\delta\omega_q \equiv \omega'_q - \omega_q = 2\chi n, \chi = \frac{g_c^2 \eta}{\Delta(\Delta + \eta)}. \quad (4)$$

Applying resonance driving with different powers to the SAW cavity and scanning the spectrum of qubit at the same time. According to $\eta/2\pi = -180$ MHz, we calibrated the average number of phonons $\langle n \rangle$ by frequency shift of qubit as $\langle n \rangle = \delta\omega_q/2\chi$. We adjusted the qubit's bias and measured the qubit frequency shift $\delta\omega_q$ at different coupling strengths, as shown in Fig. 4g. According to Eq. 4, with the same Δ and η , the slope of $\delta\omega_q$ versus the $\langle n \rangle$ should be proportional to g_c^2 . This is consistent with our experimental results. It also reveals another method for measuring electro-acoustic coupling.

In summary, we integrate the SAW cavity and the transmon qubit together using flip-chip assembly with indium bumps. Using this cQAD device, we observe the strong coupling between the qubit and SAW cavity and show the tunability of the coupling strength. Furthermore, we observe the ac stark shift of the qubit causing by the phonons in the SAW cavity. Comparing the characterization of SAW cavity in room temperature, we observe an improvement in the Q factor under lower temperatures. These can be explained by the smaller acoustic dissipation of 10 mK within the high-vacuum environment. Our work provides a new platform for studying cQAD and a new way to integrate them. The galvanic-connected flip-chip technology gives a modular way to optimize the qubit and mechanical modes separately. This new platform has potential applications in quantum communication and quantum computing.

ACKNOWLEDGMENTS

This work was supported by the National Natural Science Foundation of China (Grants No. 12204528, No. 92265207, No. T2121001, No. 11934018, No. 12005155, No. 11904393, No. 92065114, No. 12204528, No. 11875220, and No. 12047502), Innovation Program for Quantum Science and Technology (Grant No. 2021ZD0301800), and Scientific Instrument Developing Project of Chinese Academy of Sciences (Grant No. YJKYYQ20200041). Z.H. Peng also acknowledges the funding support by the National Natural Science Foundation of China (Grant No. 12074117, No. 92365209). J. Zhang also acknowledges the funding support by Tsinghua-Foshan Innovation Special Fund (TFISF), Innovative leading talent project of "Shuangqian plan" in Jiangxi Province, Joint Fund of Science and Technology Department of Liaoning Province and State Key Laboratory of Robotics, China (2021-KF-22-01) and Guoqiang Research Institute of Tsinghua University (20212000704). X.H. Ruan thanks for the measurement support from Xu Wang in CAS. This work also was supported by the Micro/nano Fabrication Laboratory of Synergetic Extreme Condition User Facility (SECUF). Devices were made at the Nanofabrication Facilities at the Institute of Physics, CAS in Beijing.

AUTHOR DECLARATIONS

Conflict of Interest

The authors have no conflicts to disclose.

¹Y. Chu, P. Kharel, W. H. Renninger, L. D. Burkhardt, L. Frunzio, P. T. Rakich, and R. J. Schoelkopf, "Quantum acoustics with superconducting qubits," *Science* **358**, 199–202 (2017).

- ²M. V. Gustafsson, T. Aref, A. F. Kockum, M. K. Ekström, G. Johansson, and P. Delsing, “Propagating phonons coupled to an artificial atom,” *Science* **346**, 207–211 (2014).
- ³R. Manenti, A. F. Kockum, A. Patterson, T. Behrle, J. Rahamim, G. Tancredi, F. Nori, and P. J. Leek, “Circuit quantum acoustodynamics with surface acoustic waves,” *Nature Communications* **8**, 975 (2017).
- ⁴A. N. Bolgar, J. I. Zotova, D. D. Kirichenko, I. S. Besedin, A. V. Semenov, R. S. Shaikhaidarov, and O. V. Astafiev, “Quantum Regime of a Two-Dimensional Phonon Cavity,” *Physical Review Letters* **120**, 223603 (2018).
- ⁵B. A. Moores, L. R. Sletten, J. J. Viennot, and K. W. Lehnert, “Cavity Quantum Acoustic Device in the Multimode Strong Coupling Regime,” *Physical Review Letters* **120**, 227701 (2018).
- ⁶K. J. Satzinger, Y. P. Zhong, H.-S. Chang, G. A. Peairs, A. Bienfait, M.-H. Chou, A. Y. Cleland, C. R. Conner, E. Dumur, J. Grebel, I. Gutierrez, B. H. November, R. G. Povey, S. J. Whiteley, D. D. Awschalom, D. I. Schuster, and A. N. Cleland, “Quantum control of surface acoustic wave phonons,” *Nature* **563**, 661–665 (2018).
- ⁷J. M. Kitzman, J. R. Lane, C. Undershute, P. M. Harrington, N. R. Bey-sengulov, C. A. Mikolas, K. W. Murch, and J. Pollanen, “Phononic bath engineering of a superconducting qubit,” *Nature Communications* **14**, 3910 (2023).
- ⁸A. D. O’Connell, M. Hofheinz, M. Ansmann, R. C. Bialczak, M. Lenander, E. Lucero, M. Neeley, D. Sank, H. Wang, M. Weides, J. Wenner, J. M. Martinis, and A. N. Cleland, “Quantum ground state and single-phonon control of a mechanical resonator,” *Nature* **464**, 697–703 (2010).
- ⁹J.-M. Pirkkalainen, S. U. Cho, J. Li, G. S. Paraoanu, P. J. Hakonen, and M. A. Sillanpää, “Hybrid circuit cavity quantum electrodynamics with a micromechanical resonator,” *Nature* **494**, 211–215 (2013).
- ¹⁰E. A. Wollack, A. Y. Cleland, R. G. Gruenke, Z. Wang, P. Arrangoiz-Arriola, and A. H. Safavi-Naeini, “Quantum state preparation and tomography of entangled mechanical resonators,” *Nature* **604**, 463–467 (2022).
- ¹¹N. R. Lee, Y. Guo, A. Y. Cleland, E. A. Wollack, R. G. Gruenke, T. Maki-hara, Z. Wang, T. Rajabzadeh, W. Jiang, F. M. Mayor, P. Arrangoiz-Arriola, C. J. Sarabalis, and A. H. Safavi-Naeini, “Strong dispersive coupling between a mechanical resonator and a fluxonium superconducting qubit,” *PRX Quantum* **4**, 040342 (2023).
- ¹²R. Manenti, M. J. Peterer, A. Nersisyan, E. B. Magnusson, A. Patterson, and P. J. Leek, “Surface acoustic wave resonators in the quantum regime,” *Physical Review B* **93**, 041411 (2016).
- ¹³A. L. Emser, B. C. Rose, L. R. Sletten, P. Aramburu Sanchez, and K. W. Lehnert, “Minimally diffracting quartz for ultra-low temperature surface acoustic wave resonators,” *Applied Physics Letters* **121**, 224001 (2022).
- ¹⁴A. Blais, A. L. Grimsmo, S. M. Girvin, and A. Wallraff, “Circuit quantum electrodynamics,” *Rev. Mod. Phys.* **93**, 025005 (2021).
- ¹⁵X. Gu, A. F. Kockum, A. Miranowicz, Y.-x. Liu, and F. Nori, “Microwave photonics with superconducting quantum circuits,” *Physics Reports* **718–719**, 1–102 (2017).
- ¹⁶A. Bienfait, K. J. Satzinger, Y. P. Zhong, H.-S. Chang, M.-H. Chou, C. R. Conner, É. Dumur, J. Grebel, G. A. Peairs, R. G. Povey, and A. N. Cleland, “Phonon-mediated quantum state transfer and remote qubit entanglement,” *Science* **364**, 368–371 (2019).
- ¹⁷C. T. Hann, C.-L. Zou, Y. Zhang, Y. Chu, R. J. Schoelkopf, S. M. Girvin, and L. Jiang, “Hardware-Efficient Quantum Random Access Memory with Hybrid Quantum Acoustic Systems,” *Physical Review Letters* **123**, 250501 (2019).
- ¹⁸M. Forsch, R. Stockill, A. Wallucks, I. Marinković, C. Gärtner, R. A. Norte, F. van Otten, A. Fiore, K. Srinivasan, and S. Gröblacher, “Microwave-to-optics conversion using a mechanical oscillator in its quantum ground state,” *Nature Physics* **16**, 69–74 (2020).
- ¹⁹M. Mirhosseini, A. Sipahigil, M. Kalaei, and O. Painter, “Quantum transduction of optical photons from a superconducting qubit,” *Nature* **588**, 599–603 (2020).
- ²⁰X. Han, W. Fu, C.-L. Zou, L. Jiang, and H. X. Tang, “Microwave-optical quantum frequency conversion,” *Optica* **8**, 1050 (2021).
- ²¹Y. Chu, P. Kharel, T. Yoon, L. Frunzio, P. T. Rakich, and R. J. Schoelkopf, “Creation and control of multi-phonon Fock states in a bulk acoustic-wave resonator,” *Nature* **563**, 666–670 (2018).
- ²²L. R. Sletten, B. A. Moores, J. J. Viennot, and K. W. Lehnert, “Resolving Phonon Fock States in a Multimode Cavity with a Double-Slit Qubit,” *Physical Review X* **9**, 021056 (2019).
- ²³H. Qiao, É. Dumur, G. Andersson, H. Yan, M.-H. Chou, J. Grebel, C. R. Conner, Y. J. Joshi, J. M. Miller, R. G. Povey, X. Wu, and A. N. Cleland, “Splitting phonons: Building a platform for linear mechanical quantum computing,” *Science* **380**, 1030–1033 (2023).
- ²⁴G. Andersson, B. Suri, L. Guo, T. Aref, and P. Delsing, “Non-exponential decay of a giant artificial atom,” *Nature Physics* **15**, 1123–1127 (2019).
- ²⁵G. Andersson, M. K. Ekström, and P. Delsing, “Electromagnetically Induced Acoustic Transparency with a Superconducting Circuit,” *Physical Review Letters* **124**, 240402 (2020).
- ²⁶G. Andersson, S. W. Jolin, M. Scigliuzzo, R. Borgani, M. O. Tholén, J. Rivera Hernández, V. Shumeiko, D. B. Haviland, and P. Delsing, “Squeezing and Multimode Entanglement of Surface Acoustic Wave Phonons,” *PRX Quantum* **3**, 010312 (2022).
- ²⁷W. Jiang, J. Chen, X. Liu, Z. Niu, K. Liu, W. Peng, Z. Wang, and Z.-R. Lin, “Thin film aluminum nitride surface acoustic wave resonators for quantum acoustodynamics,” *Applied Physics Letters* **123**, 024002 (2023).
- ²⁸X.-B. Xu, J.-Q. Wang, Y.-H. Yang, W. Wang, Y.-L. Zhang, B.-Z. Wang, C.-H. Dong, L. Sun, G.-C. Guo, and C.-L. Zou, “High-frequency traveling-wave phononic cavity with sub-micron wavelength,” *Applied Physics Letters* **120**, 163503 (2022).
- ²⁹R. Manenti, M. J. Peterer, A. Nersisyan, E. B. Magnusson, A. Patterson, and P. J. Leek, “Surface acoustic wave resonators in the quantum regime,” *Physical Review B* **93**, 041411 (2016).
- ³⁰D. Morgan, *Surface Acoustic Wave Filters: With Applications to Electronic Communications and Signal Processing(second edition)* (Academic Press, Oxford, 2007).
- ³¹L. B. Ioffe, V. B. Geshkenbein, C. Helm, and G. Blatter, “Decoherence in superconducting quantum bits by phonon radiation,” *Physical Review Letters* **93**, 057001 (2004).
- ³²Y. Chen, C. Neill, P. Roushan, N. Leung, M. Fang, R. Barends, J. Kelly, B. Campbell, Z. Chen, B. Chiaro, A. Dunsworth, E. Jeffrey, A. Megrant, J. Y. Mutus, P. J. J. O’Malley, C. M. Quintana, D. Sank, A. Vainsencher, J. Wenner, T. C. White, M. R. Geller, A. N. Cleland, and J. M. Martinis, “Qubit Architecture with High Coherence and Fast Tunable Coupling,” *Physical Review Letters* **113**, 220502 (2014).
- ³³M. R. Geller, E. Donate, Y. Chen, M. T. Fang, N. Leung, C. Neill, P. Roushan, and J. M. Martinis, “Tunable coupler for superconducting Xmon qubits: Perturbative nonlinear model,” *Physical Review A* **92**, 012320 (2015).
- ³⁴M. Datta, “Microelectronic packaging trends and the role of nanotechnology,” in *Electrochemical Nanotechnologies* (Springer New York, New York, NY, 2010) pp. 227–253.
- ³⁵B. Foxen, J. Y. Mutus, E. Lucero, R. Graff, A. Megrant, Y. Chen, C. Quintana, B. Burkett, J. Kelly, E. Jeffrey, Y. Yang, A. Yu, K. Arya, R. Barends, Z. Chen, B. Chiaro, A. Dunsworth, A. Fowler, C. Gidney, M. Giustina, T. Huang, P. Klimov, M. Neeley, C. Neill, P. Roushan, D. Sank, A. Vainsencher, J. Wenner, T. C. White, and J. M. Martinis, “Qubit compatible superconducting interconnects,” *Quantum Science and Technology* **3**, 014005 (2018).
- ³⁶K. Wade and A. J. Banister, *The chemistry of aluminium, gallium, indium and thallium* (Elmsford, NY: Pergamon Press, 1975).
- ³⁷K. Shibayama, K. Yamanouchi, H. Sato, and T. Meguro, “Optimum cut for rotated y-cut linbo3crystal used as the substrate of acoustic-surface-wave filters,” *Proceedings of the IEEE* **64**, 595–597 (1976).